The impact of a realistic vertical dust distribution on the simulation of the Martian General Circulation

Scott D. Guzewich,[1] Anthony D. Toigo,[2] Mark I. Richardson,[3] Claire E. Newman,[3] Elsayed R. Talaat,[2] Darryn W. Waugh,[4] and Timothy H. McConnochie[5]

Received 8 February 2013; revised 5 April 2013; accepted 20 April 2013; published 20 May 2013.

[1] Limb-scanning observations with the Mars Climate Sounder and Thermal Emission Spectrometer (TES) have identified discrete layers of enhanced dust opacity well above the boundary layer and a mean vertical structure of dust opacity very different from the expectation of well-mixed dust in the lowest 1–2 scale heights. To assess the impact of this vertical dust opacity profile on atmospheric properties, we developed a TES limb-scan observation-based three-dimensional and time-evolving dust climatology for use in forcing general circulation models (GCMs). We use this to force the MarsWRF GCM and compare with simulations that use a well-mixed (Conrath-ν) vertical dust profile and Mars Climate Database version 4 (MCD) horizontal distribution dust opacity forcing function. We find that simulated temperatures using the TES-derived forcing yield a 1.18 standard deviation closer match to TES temperature retrievals than a MarsWRF simulation using MCD forcing. The climatological forcing yields significant changes to many large-scale features of the simulated atmosphere. Notably the high-latitude westerly jet speeds are 10–20 m/s higher, polar warming collar temperatures are 20–30 K warmer near northern winter solstice and tilted more strongly poleward, the middle and lower atmospheric meridional circulations are partially decoupled, the migrating diurnal tide exhibits destructive interference and is weakened by 50% outside of equinox, and the southern hemisphere wave number 1 stationary wave is strengthened by up to 4 K (45%). We find the vertical dust distribution is an important factor for Martian lower and middle atmospheric thermal structure and circulation that cannot be neglected in analysis and simulation of the Martian atmosphere.

Citation: Guzewich, S. D., A. D. Toigo, M. I. Richardson, C. E. Newman, E. R. Talaat, D. W. Waugh, and T. H. McConnochie (2013), The impact of a realistic vertical dust distribution on the simulation of the Martian General Circulation, *J. Geophys. Res. Planets*, *118*, 980–993, doi:10.1002/jgre.20084.

1. Introduction

[2] The importance of dust in the Martian atmosphere was suggested before spacecraft visited the planet [*Sagan and Pollack*, 1969]. The dramatic observations of the 1971 global dust storm by Mariner 9 cemented dust's dominant role in Martian atmospheric dynamics through radiative-dynamic coupling. Mariner 9 observed dust uniformly mixed to heights of 40–50 km altitude and dramatic heating of the atmosphere by dust during and immediately after this major storm event [*Leovy et al.*, 1972; *Hanel et al.*, 1972].

[3] Improved understanding of dust's role in the radiative-dynamic balance that drives the Martian climate over seasonal cycles has been obtained through multiannual observations from the Viking orbiters [e.g., *Martin*, 1981], the Viking landers [e.g., *Pollack et al.*, 1979; *Zurek and Leovy*, 1981], and more recently by Mars Global Surveyor (MGS) [*Smith et al.*, 2001; *Smith*, 2004] and the Mars Reconnaissance Orbiter (MRO) [*McCleese et al.*, 2008]. Dust provides a very significant modulation of the thermal forcing of the atmosphere, including a significant amplification of the difference between the northern and southern summer solstice periods, which is ultimately due to the near coincidence of northern summer solstice ($L_s = 90°$) with aphelion (at $L_s = 71°$), Mars' large eccentricity [e.g., *Colburn et al.*, 1989] and the hemispheric topographic dichotomy [*Richardson and Wilson*, 2002].

[4] Observational and general circulation modeling (GCM) studies confirm that dust is a key forcing mechanism through the absorption of solar radiation and the absorption and emission of planetary thermal radiation, primarily in the 8–12 μm silicate band. Dynamical consequences of this radiative forcing include large thermal tides [*Leovy and Zurek*, 1979; *Zurek and Leovy*, 1981, *Wilson and Hamilton*, 1996], strong modulation of the strength of the meridional

[1]NASA Goddard Spaceflight Center, Greenbelt, Maryland, USA.
[2]The Johns Hopkins University Applied Physics Laboratory, Laurel, Maryland, USA.
[3]Ashima Research, Pasadena, California, USA.
[4]Department of Earth and Planetary Sciences, Johns Hopkins University, Baltimore, Maryland, USA.
[5]Department of Astronomy, University of Maryland, College Park, Maryland, USA.

Corresponding author: S. D. Guzewich, NASA Goddard Spaceflight Center, 8800 Greenbelt Rd., Bldg. 34 Greenbelt, MD 20771, USA. (scott.d.guzewich@nasa.gov)

©2013. American Geophysical Union. All Rights Reserved.
2169-9097/13/10.1002/jgre.20084

Hadley circulation [*Haberle et al*., 1982; *Haberle et al*., 1993], and a significant winter polar warming during dust storms [*Deming et al*., 1986; *Jakosky and Martin*, 1987; *Wilson*, 1997; *Bell et al*., 2007; *Kuroda et al*., 2009]. These studies show that increased dust loading of the atmosphere results in stronger radiative forcing and a more vigorous circulation, which manifests as a deepened and expanded Hadley circulation and a more intense (as represented by temperature amplitude) polar warming. That picture is more complex for thermal tides and waves, with different waves exhibiting unique responses to increased dust loading. For example, the migrating diurnal and semidiurnal tides are strengthened during dust storms and periods of higher dust loading [*Zurek and Leovy*, 1981], while the diurnal Kelvin wave's amplitude remains relatively invariant [*Wilson and Hamilton*, 1996].

[5] While the study of the impact of the bulk amount of dust in the atmosphere on thermal structure and circulation has received a great deal of attention, comparatively little work has been done to identify the impact of the vertical and horizontal distribution of dust on dynamical properties of the atmosphere. Many Mars GCMs utilize the Conrath-ν dust profile [*Conrath*, 1975] in the vertical dimension and use horizontal distributions designed to mimic spacecraft observations of dust and/or temperature to a greater or lesser extent (see, e.g., the various "dust scenarios" used in simulations for the Mars Climate Database (MCD) [*Lewis et al*., 1999]). However, no published Mars GCMs ingest spacecraft observations directly (with the notable exception of data assimilation experiments). The Conrath-ν profile is an idealized representation in the vertical dimension of a hypothesized balance between vertical eddy mixing of dust and gravitational sedimentation and was formulated to best match the Mariner 9 observations during the decay of a global dust storm. A "modified" Conrath-ν profile has also been developed [e.g., *Montmessin et al*., 2004] which varies the effective top of the dust in the atmosphere seasonally and spatially. Other Mars GCM experiments have examined the role of dynamically interactive dust, meaning that radiatively active dust is transported by prognostic model winds, with dust lifting often also parameterized in terms of the evolving atmospheric state. *Murphy et al*. [1993], *Wilson and Hamilton* [1996], *Newman et al*. [2002a; 2002b], *Basu et al*. [2004], and *Kahre et al*. [2006, 2008] have examined the importance of feedbacks between dust and the circulation on such topics as the size segregation of dust particles, the ability to adequately simulate thermal tides, the development of regional and global dust storms, and the net transport of dust. Generally, these simulations suggested only a modest deviation from a well-mixed lower atmosphere outside of dust storms, and in combination with a lack of observations to contradict the Conrath-ν profile, the well-mixed lower atmosphere profile has seen broad adoption by the Mars GCM community, as well as in the retrieval of nadir observations from IRTM and TES [*Smith et al*., 2001]. More recent studies have found that the use of a Conrath-ν profile or modified Conrath-ν profile is insufficient to match observed temperatures and recommend the use of fully or partially interactive dust to improve GCM simulations of temperature observations [*Kahre et al*., 2008; *Wilson et al*., 2008; *Madeleine et al*., 2011; *Greybush et al*., 2012]. As suggested by *Heavens et al*. [2011a], however, the inability of current GCMs—even with fully interactive dust—to predict the dust vertical distributions observed by TES (limb) and MCS implies that fundamental physical processes controlling the dust distribution are missing from the models. As such, the use of prescribed forcing based on TES limb observations is likely to yield a more accurate forcing of the model atmosphere than either fully or forcing of GCMs with data assimilation of TES nadir retrievals or radiances (which intrinsically contain no or little interactive dust modeling information on vertical distribution, respectively) [*Lee et al*., 2009; *Greybush et al*., 2012].

[6] Recent limb observations by the Mars Climate Sounder (MCS) [*Heavens et al*., 2011a; 2011b] and the Thermal Emission Spectrometer (TES) [*Clancy et al*., 2010; *Guzewich et al*., 2013] have shown that the traditional and modified Conrath-ν profiles are a poor fit in some seasons and locations, particularly when discrete layers of enhanced dust mixing ratios are seen in the Martian low latitudes. Here we use the nearly 3 Mars year (MY) limb-scanning observations of dust by TES, showing two discrete layers of locally high dust mixing ratios (particularly in the low latitudes, see *Guzewich et al*. [2013] for details), to radiatively force the MarsWRF GCM [*Richardson et al*., 2007; *Toigo et al*., 2012] and determine the impact of an empirically derived vertical dust profile on the simulated Martian atmosphere. Section 2 describes our methodology, describing the six GCM simulations we conducted and how comparisons of those simulations were used to draw our conclusions. Section 3 analyzes the impact to the general circulation in terms of the temperature and wind fields, the polar warming and the mean meridional circulation produced. Section 4 analyzes the impact to thermal tides and planetary waves, and section 5 concludes the work.

2. Methodology

[7] MarsWRF is a numerical atmospheric model that has been developed through modification of the terrestrial Weather Research and Forecasting (WRF) mesoscale model [*Richardson et al*., 2007; *Toigo et al*., 2012]. MarsWRF is capable of running on a variety of platforms at various resolutions, allowing atmospheric processes to be examined at the microscale, mesoscale and global scales, and of connecting the different scales in the same simulation through interactive "nesting" of areal domains. All of the experiments conducted in this work were carried out at global scales only, where MarsWRF acts as a GCM. Specification of dust properties and amounts in MarsWRF is a selectable input option. The available treatments include (A) uniform, fixed column optical depth, where a single value of optical depth at a reference pressure of 610 Pa is specified, and dust is distributed in the vertical following the Conrath-ν profile; (B) time and space varying total column optical depth opacity based on either the "MGS scenario" or the "Viking scenario" of the MCD version 4 [*Lewis et al*., 1999; *Montmessin et al*., 2004; *Toigo et al*., 2012], with the former scenario representing the MGS TES MY 24 nadir-based observations, and the latter representing the Viking Lander years with the global dust storms removed; and (C) fully dynamically and radiatively interactive dust using two particle size bins and prognostic dust lifting. For all previous studies, except those specifically focused on the dust cycle,

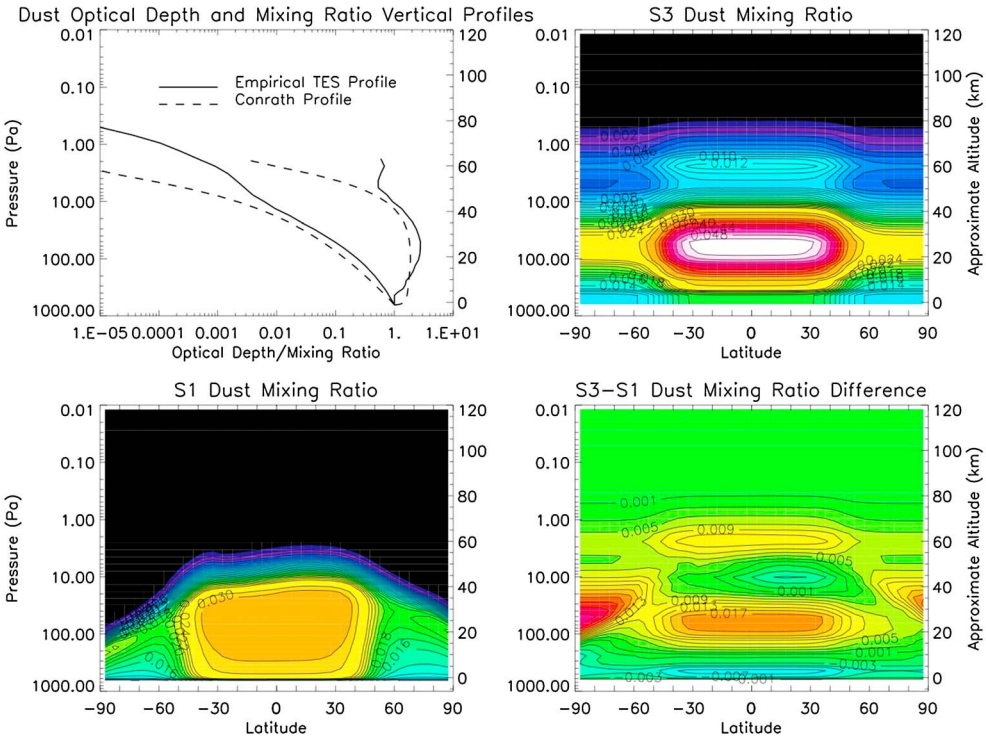

Figure 1. (a) A comparison of the average dust optical depth vertical profiles used in this study (left two lines) and dust mixing ratio (optical depth per mb, right two lines). A modified Conrath-ν vertical dust profile (dashed line) [*Conrath*, 1975; *Montmessin et al*., 2004] was used in simulations S1 and S4, while the empirically derived TES limb vertical dust profile (solid line) [*Guzewich et al*., 2013] was used in simulations S2 and S3. (b) Dust mixing ratio for S3, (c) dust mixing ratio for S1, and (d) the difference between the two. All plots for $L_s = 0°$.

MarsWRF has typically been run with option B. Option B uses the "modified" Conrath-ν profile of *Montmessin et al*. [2004] which includes a seasonally and latitudinally varying "top of effective dust" (z_{max}) parameter and a Conrath parameter (ν) of 0.007. We used the MarsWRF wideband model (WBM) radiative heating option, which is computationally efficient and extensively calibrated for the current climate. The WBM scheme treats CO_2 in the thermal infrared and solar bands following *Hourdin* [1992] and *Forget et al*. [1999]. Dust radiative heating is treated by the WBM scheme following *Briegleb* [1992] for the solar and *Haberle et al*. [1982] for the thermal infrared. We use a single band for solar and a single band for the thermal infrared. The same schemes have been used in the GFDL/SKYHI Mars GCM [*Wilson and Richardson*, 2000] and the Mars MM5 model [*Toigo and Richardson*, 2002], as well as in past MarsWRF simulations [*Richardson et al*., 2007; *Toigo et al*., 2012].

[8] The dust radiative properties used to produce these results were taken from *Haberle et al*. [1982] in the thermal infrared and *Clancy et al*. [1995] in the visible. These have a long history of use in the GFDL/SKYHI Mars GCM [*Wilson and Richardson*, 2000], Mars MM5 [*Toigo and Richardson*, 2002], and prior MarsWRF simulations [*Richardson et al*., 2007; *Toigo et al*., 2012]. Given the low spectral resolution of the WBM radiative transfer scheme (one band for solar, one band for the thermal infrared), inclusion of recent high-resolution dust properties [*Wolff et al*., 2009] was not possible, though future work will be conducted using a modern, high-spectral resolution radiative transfer code (the KDM scheme described in *Mischna et al*. [2012]) enabling the most recent dust and ice radiative properties to be included.

[9] However, even if such radiative properties are used, this does not ensure complete realism in terms of the vertical heating distribution. This would require that dust particle sizes also vary realistically in the vertical, opacity varies realistically in local time (currently it is poorly known away from the local times of the observations), and water ice cloud radiative effects be included. Rather than including every possible effect at once, the intention of the present study is to isolate and examine the impact of changing the vertical dust distribution (relative to the impact of changes in the total column optical depth and horizontal dust prescription), much as the impact of including water ice cloud radiative effects has been isolated and investigated in other studies [e.g., *Madeleine et al*., 2012]. The past usage history and simplicity of our chosen radiative transfer schemes also allow us to limit the complexity of the interpretation and permit more direct comparison with past simulations performed with MarsWRF and other models.

[10] Using the TES limb-scanning observations described in *Guzewich et al*. [2013], we created a family of dust climatologies suitable for use in MarsWRF, specifying the distribution of dust in both the horizontal and vertical. Two options were created: a fully time-evolving, 3 MY duration dust scenario to mimic the observed MY 24–27 period and an "annual average" dust scenario that uses the median dust optical depth value from the same 3 year period. These

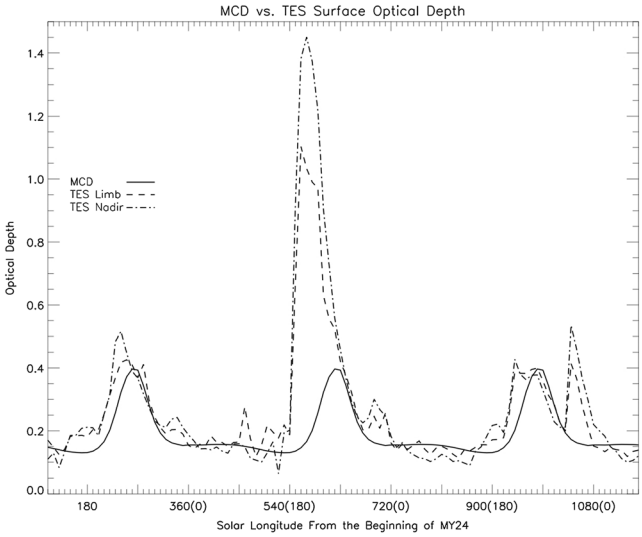

Figure 2. A comparison of area-weighted global average total column optical depth from the MCD (solid line), TES limb scan observations (dashed line) and TES nadir scan observations (dash-dotted line) for the nearly 3 MY period (MY 24–27) of TES limb scans discussed in *Guzewich et al*. [2013]. The large perturbation caused by the global dust storm of 2001 can be seen near the center of the figure.

scenarios were created by interpolating the coarser-resolution TES observations onto the WRF spatial grid. Differences between 1400 and 0200 local solar time observations by TES were interpolated across local time with a sinusoid. Spatial data gaps were interpolated horizontally between neighboring latitude and longitude bins. Large temporal gaps were filled by another Mars year's observations. In high-opacity situations, the low-altitude TES limb observations are considered unreliable (see *Guzewich et al*. [2013] for details) and a Conrath-ν profile was instead fitted from the lowest reliable bin to the local surface. Total column opacity in a given (longitude, latitude, time) bin was normalized to the concurrently observed TES-nadir observations.

[11] Additionally, an empirical "TES vertical dust profile" was calculated by casting each TES limb-scan observation as a normalized profile (as a function of height) relative to the total column optical depth, and then averaging the full set of normalized profiles. This empirical TES profile was designed to be used as a substitute for the modified Conrath-ν vertical profile typically used by the GCM. Figure 1 compares this TES vertical dust profile to a modified Conrath-ν dust profile, with total column opacity and mixing ratio normalized to 1. In brief, the key features of the empirical TES profile that differentiate it from the modified Conrath-ν profile are the presence of the two discrete layers of enhanced dust mixing ratio at 20–30 km and again at 45–65 km, as described by *Guzewich et al*. [2013]. The lower layer was first identified by *Heavens et al*. [2011a] and is referred to as the "lower dust maximum" (LDM) in *Guzewich et al*. [2013]. These layers can be visually identified as the two "shoulders" or "bumps" in the empirical TES optical depth and mixing ratio profiles in Figure 1a. Figures 1b–1d also show the differences (in dust mixing ratio) between zonal averages (latitude versus height) of the two dust profiles. Figure 2 compares the area-weighted total column optical depths of the MCD MGS scenario (solid line), the TES limb-derived (dashed line), and TES nadir-derived (dash-dot line) maps (see *Guzewich et al*. [2013] for additional information on the TES observations). There is no systematic bias for the TES values to be larger or smaller than the MCD, which is to be expected given that the MCD MGS scenario was developed to approximate MY 24 TES nadir observations. Any significant changes in optical depth from the MCD MGS scenario values are due to particular events such as the 2001 global dust storm (hereafter GDS01).

[12] We analyzed six MarsWRF simulations for this study, outlined in Table 1. All simulations were run with 5° horizontal grid spacing and with 40 vertical levels ("standard resolution" as defined by *Toigo et al*. [2012]). The first simulation (S1) used the MGS scenario described above and in *Montmessin et al*. [2004] and thus utilized a "modified" Conrath-ν vertical dust opacity profile. This simulation mainly served as a baseline reference case. The second simulation (S2) utilized TES limb-scan observations to specify the model horizontal dust distribution using the climatological (3 year) average of the TES limb data and then the vertical dust profile at each grid point in the model was exactly specified using the empirical TES vertical profile adjusted to the local total column dust opacity. The total column dust opacity used was the TES nadir-derived column opacity appropriate to that time and spatial location, with an adjustment factor of 1.3 to include scattering [*Smith*, 2004]. The third simulation (S3) was a hybrid of the first two, utilizing the same total optical depth values in the horizontal as S1 (from the "MGS scenario"), but employing the empirical TES vertical profile. The fourth (S4) was also a hybrid, but in the opposite sense to S3: it instead used the TES nadir-derived column opacities with a modified Conrath-ν vertical profile. These first four simulations were all initialized from long-term average climatological initial conditions and run for 2 Mars years, with the first year then rejected to avoid any "spin-up" issues (i.e., transient behavior as the GCM adjusted to the dust forcing). The fifth simulation (S5) was similarly initialized, then run for approximately 3 MY and utilized the entire TES limb-scan observation dust profile database (i.e., the TES limb climatology from MY 24–27 was "replayed" through the GCM forcing in order to examine year-over-year differences). In S5, the vertical dust profile evolved as the observed TES limb climatology dictated. The sixth and final simulation (S6) used an entirely dust-free atmosphere as an additional baseline reference case. Simulations S2–S4 were conducted primarily to differentiate the impact of the vertical dust profile change with that of the different surface dust optical depth

Table 1. MarsWRF Simulations

Simulation	Length (Mars Years)	Horizontal Resolution (Degrees)	Total Optical Depth Source Data Set	Vertical Dust Profile
1	1	5	MCD MGS	Conrath-ν
2	1	5	TES Average	TES Average
3	1	5	MCD MGS	TES Average
4	1	5	TES Average	Conrath-ν
5	3	5	TES Climo.	TES Climo.
6	1	5	No Dust	N/A

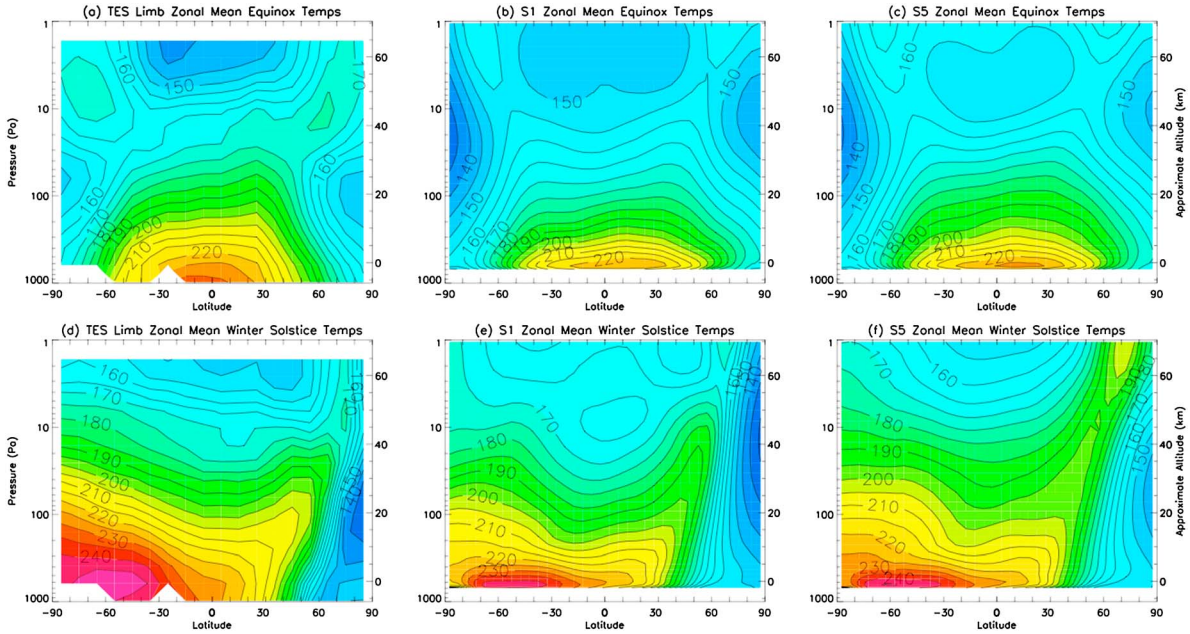

Figure 3. Zonal mean temperatures (Kelvin) averaged over the (top) equinox seasons ($L_s = 0°$ and $L_s = 180°$) and (bottom) northern winter solstice ($L_s = 270°$) for the (a, d) TES limb-scan observations and simulations (b, e) S1 and (c, f) S5. Multiple years are averaged together for the TES limb-scan observations and simulation S5.

distributions (TES nadir-derived total column opacity versus that of the MGS scenario) when analyzing simulation S5. Given the lack of bias between the two optical depth distributions (as seen in Figure 2), for a given period where the TES-derived total column optical depths and MGS scenario total column optical depths are similar on a globally averaged basis, we interpret differences in the simulated meteorological fields as either due to the altered vertical dust profile or the altered longitudinal and latitudinal distribution of total column optical depth. To differentiate these two potential factors and ascertain the impact of the altered vertical dust profile, we can compare simulations with identical total column optical depth maps (i.e., compare simulations S1 and S4 and compare simulations S2 and S3).

3. Impact on General Circulation

3.1. Temperatures and Winds

[13] We first evaluate the changes in the dust profile by comparing modeled temperatures to the TES observations. The model output was interpolated to match our TES data binning structure (see *Guzewich et al*. [2013] for details) in all three spatial dimensions and time, and the arithmetic difference was taken and then averaged globally with appropriate area weighting. Our simulation S5 of MY 24–27 yielded a mean temperature departure of 0.46 K compared to −4.09 K from simulation S1 using the MCD MGS/modified Conrath-ν dust scenario. Assuming a Gaussian profile around the mean of −4.09 K difference (as represented by the S1 simulated temperatures minus the TES limb observed temperatures), this represents a 1.18 standard deviation change. In an absolute sense, the TES dust scenario resulted in a 1.02 K improvement over the MCD MGS/modified Conrath-ν dust scenario, with the improvement reduced to 0.67 K if the two large dust events (the 2001/MY 25 global dust storm and the MY 26 late-year flushing event) were not included.

[14] Most of this improvement comes from more accurate representations of two particular features of the atmospheric temperature field: the tropical lower atmosphere and the polar warmings. TES observations of the tropical lower atmosphere (10–40 km altitude) during the second half of the Martian year are typically 5–20 K warmer than depicted in our "standard" MarsWRF simulation S1 using the MCD MGS/modified Conrath-ν dust scenario (Figures 3a and 3b). Our simulation S5 of MY 24–27 with the full TES dust climatology reduces this error to 0–10 K in most cases (Figure 3c). This improvement is the result of the presence of the LDM in the vertical dust profiles of the 3 year TES dust climatology. Increased optical depth at this altitude range results in greater heating and warming at this altitude level in simulation S5, and also in simulation S3, which uses MCD MGS (rather than TES) total column optical depths but does utilize the empirical TES vertical profile. The tropical lower atmosphere in simulation S3 (not shown in Figure 3) is approximately 5 K warmer than that depicted for simulation S1. A similar result is seen in simulation S2. A warm (warmer than simulated in S1) tropical lower atmosphere has also been observed by MCS. *McCleese et al.* [2010] noted comparably warm temperatures to TES during the second half of the Martian year in the lower altitude tropics (see their Figures 4 and 5).

[15] The match to observations in the tropical middle atmosphere (50+ km) is not as good as that in the lower atmosphere (more poorly depicted) for simulations S5, S3, and (to a lesser degree) S1. TES limb-scanning observations indicate sub-140 K temperatures in the tropical atmosphere near 50 km altitude during northern spring and summer

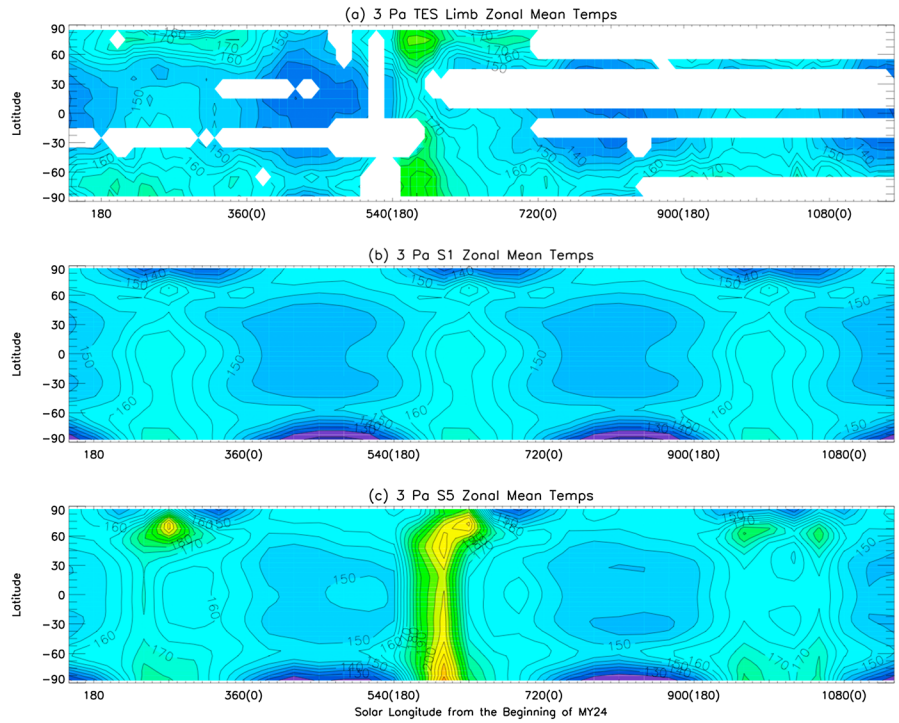

Figure 4. (a) TES limb-scan temperatures observations interpolated to 3 Pa compared with temperatures output by (b) simulation S1 and (c) simulation S5.

($L_s = 0°–180°$, Figure 4a). Again, similar temperatures have been seen with MCS [*McCleese et al.*, 2010]. For the same time period and location, simulation S1 is approximately 10 K warmer than the TES observations and simulation S5 is up to an additional 5 K warmer still (Figures 4b and 4c). The presence of enhanced optical depths in the empirical TES climatology provides additional warming and produces this additional 0–5 K temperature anomaly beyond what simulation S1 already shows. As *Heavens et al.* [2011c] and others have discussed, the cold tropical middle atmosphere is likely due to intense adiabatic cooling in the ascending branch of the Hadley circulation. It is apparent from simulation S1 that the simulated dynamics in this location are not accurately representing this feature of the circulation, but the departure is even greater when the additional heating (that must be balanced by adiabatic cooling in the real Martian atmosphere) from the 45–65 km dust layer is included.

[16] We note that recent studies have found that the radiative effect of water ice clouds could also warm the lower atmosphere during the day when clouds absorb surface-emitted radiation, as dust does in our simulations. At night, as noted in *Guzewich et al.* [2013], TES limb observations indicate clouds at the same altitudes as the LDM (at least at the ~2 A.M. observation time), and while locations within clouds are significantly cooled then by emission, the surrounding atmospheric (and surface) layers may be warmed at night, as described by *Wilson et al.* [2008] and *Madeleine et al.* [2012]. In the tropical middle atmosphere during the first half of the year, it should also be noted that water ice clouds are present and at optical depths that are higher than at any other time during the year. It is at least plausible that the failure of the model to adequately simulate the very cold tropical middle atmosphere during this period is associated with the presence of ice cloud radiative forcing that is not considered in this version of the model. Both of the studies mentioned indicated cooling from water ice clouds at altitudes of 50–60 km (see Figure 3c of *Wilson et al.* [2008] and Figure 2a of *Madeleine et al.* [2012]). Ice clouds are beyond the scope of this paper, but have been retrieved from both TES limb and MCS data, and their impact on forcing will be the subject of a forthcoming paper.

[17] Through the thermal wind relation, the zonal mean winds and their vertical shear are intimately tied to the horizontal temperature field. In nearly all seasons, the tropical lower and middle atmosphere is warmer in simulations S2 and S3 (both of which use an empirical TES vertical dust profile) than simulations S1 and S4 (both of which use a modified Conrath-ν profile). This drives a greater westerly acceleration of the zonal mean winds in nearly all seasons in simulations S2 and S3, resulting in westerly jet cores 10–20 m/s faster (Figure 5). Conversely, near $L_s = 270°$ (northern winter solstice), the stronger Hadley circulation provides a strong easterly acceleration and forces a stronger eastward jet in the tropics and southern hemisphere that is up to 80 m/s faster than its modified Conrath-ν counterpart. Comparing modeled winds to observed temperature-derived gradient winds (or making comparisons between different temperature-derived data sets) has been generally unsuccessful, but is the only available method until a (much needed) direct wind observation instrument is employed at Mars. Using TES, *Smith et al.* [2001] derived a >100 m/s gradient wind jet core in the northern hemisphere at $L_s = 180°$. *McCleese et al.* [2010] derived similar speeds with MCS; however, all of our simulations show the strongest winds in

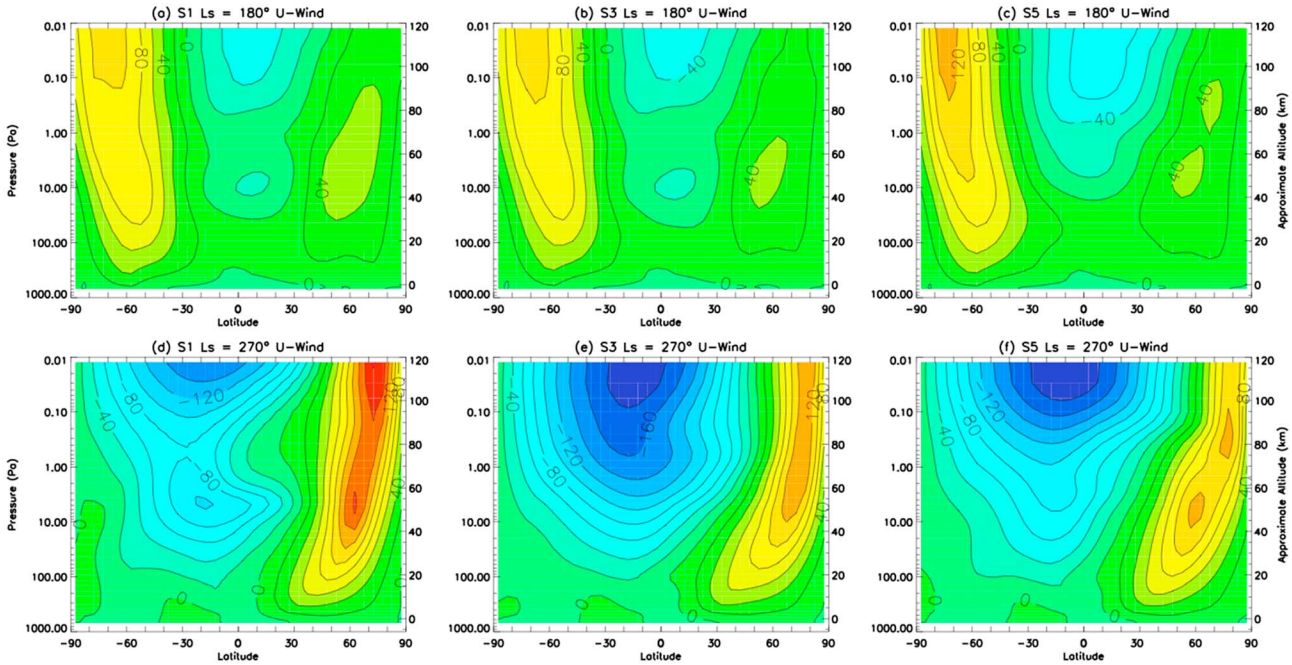

Figure 5. Zonal mean zonal winds (U-component, m/s) at (top) northern fall equinox ($L_s = 180°$) and (bottom) northern winter solstice ($L_s = 270°$) for simulations (a, d) S1, (b, e) S3, and (c, f) S5.

the southern hemisphere at this season and the shift to stronger winds in the northern hemisphere lags behind the observation-inferred winds. The comparisons are more favorable at $L_s = 270°$, where the two simulations with empirical TES dust profiles show a much larger area of easterly winds (Figures 5e and 5f), which appears consistent with *Smith et al.* [2001, see their plate 7].

[18] The mechanism for the polar warming was first clearly delineated by *Wilson* [1997] and was shown to be strongly linked to atmospheric dust loading via the amplification of thermal tides which yield sufficient wave drag to allow nearly pole-to-pole expansion of the meridional overturning circulation at upper levels (this circulation is also very deep, involving the whole atmosphere up to ~80–100 km altitude). This cell creates downwelling and adiabatic warming at middle atmospheric altitudes (~50 km) at high latitudes and consequently an intense temperature inversion above the polar vortex. What was surprising from the MCS observations (and confirmed by TES limb) is that both poles experience a modest version of polar warming throughout much of the autumn and winter seasons [*McCleese et al.*, 2008; McCleese *et al.*, 2010]. GCM simulations of this "background" or "persistent" polar warming have been of mixed success and specifically have difficulty in reproducing both the amplitude and slope (in latitude versus height space) of the polar warming in comparison to observations [*McCleese et al.*, 2008], though recently, studies have indicated that elevated water ice clouds may contribute significantly to this type of polar warming [*Wilson*, 2011; *Madeleine et al.*, 2012].

[19] The impact of dust forcing on the persistent polar warming has not been widely studied, at least partly because the MCS and TES findings are relatively new. This is the first study of the impact of an altered vertical dust profile on the persistent polar warming. To quantify the polar warming, we employ a simple metric, T_{PW}, following *McDunn et al.* [2011]:

$$T_{PW}(z) = T_{\text{hemispheric max}}(z) - T_{\text{EQ-ward min}}(z) \quad (1)$$

[20] Here T_{PW} is meant to represent the temperature amplitude of the polar warming, $T_{\text{hemispheric max}}$ is the maximum temperature in a given hemisphere at a given altitude, $T_{\text{EQ-ward min}}$ is the minimum temperature between the equator and the latitude of the hemispheric maximum temperature, and z is altitude. We evaluate T_{PW} at the 55 km altitude level using zonally averaged temperatures. Using this metric, the 3 Mars year simulation S5 using the evolving vertical dust profiles of the TES dust climatology shows a marked improvement over our simulation S1 using the MCD MGS/modified Conrath-ν dust scenario. For the northern hemisphere, the TES observations have an average polar warming index of 24.9 K, while simulation S5 has an index of 12.3 K, and simulation S1 has an index of 7.6 K. For the southern hemisphere, the TES observations have an average polar warming index of 23.1 K, simulation S5 has an index of 9 K, and simulation S1 has an index of 6.7 K.

[21] As mentioned in the previous section, the tropical middle atmosphere is generally warmer in simulation S5 than either the TES observations or simulation S1. Therefore, this improvement in the depiction of the polar warming is primarily driven by the significantly warmer polar inversion in simulations with the empirical TES vertical dust distribution (S2, S3, S5). This is seen clearly in Figure 6 which shows the zonal mean temperatures for $L_s = 270°$ for simulations S1–S4. Indeed, simulations S2, S3, and S5 (not shown) with an empirical TES dust distribution depict a polar inversion that is stronger (based on the simple polar warming index and the maximum temperature within the temperature

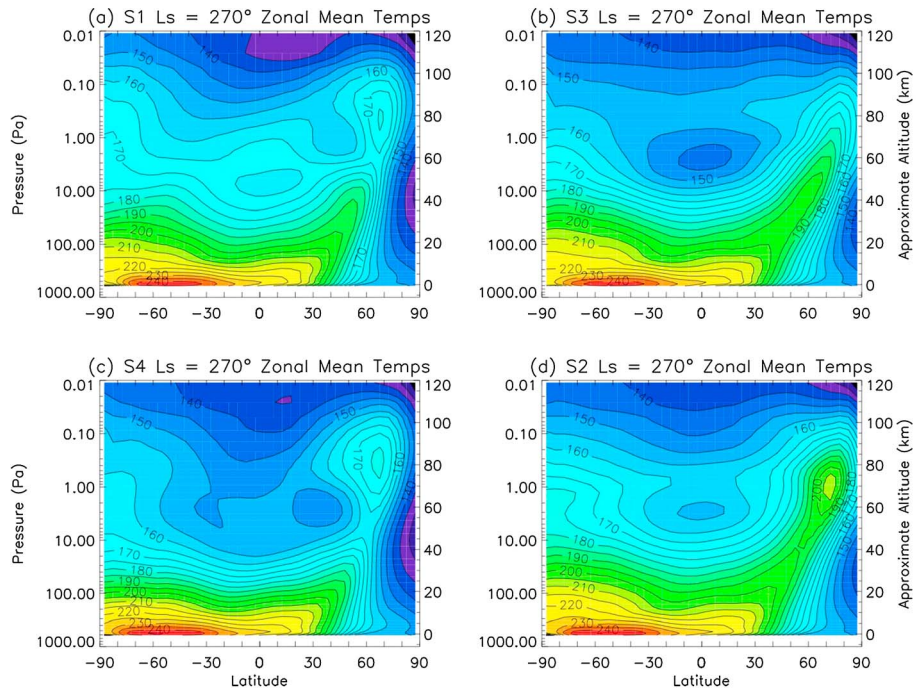

Figure 6. Zonal mean temperatures at $L_s = 270°$ (northern winter solstice) highlighting the polar warming for simulation (a) S1, (b) S3, (c) S2, and (d) S4. The right column displays the simulations with empirical TES vertical dust profiles.

inversion) than TES observations indicate (see Figure 3d for TES observations). The polar warming in these simulations is also tilted more poleward, again a closer match to observations. As the prime driver of the polar warming is adiabatic warming in the downwelling branch of the meridional circulation, the improved depiction of the polar warming is an indicator of a more realistic depiction of the meridional circulation. As will be discussed in section 3.2, we believe this more realistic depiction of the meridional circulation is due to the presence of the LDM in the empirical TES vertical dust profile.

3.2. Mean Meridional Circulation

[22] Using the Transformed Eulerian Mean framework (TEM) [*Andrews and McIntyre*, 1976], we analyzed the residual mean meridional circulation of the simulations. In this section, we highlight comparisons between simulations S1 and S3, both of which used the MCD MGS total column dust optical depth distributions, but which utilized the modified Conrath-ν and empirical TES vertical dust profiles, respectively. Figure 7 compares the two circulations at $L_s = 330°$ (averaged over 30° of solar longitude centered on 330°). The combined circulation is deeper in the simulation with the empirical dust profile, despite the Hadley circulation at low altitudes being comparable or slightly weaker in amplitude than the simulation with the modified Conrath-ν profile. By altering the vertical dust profile, the residual mean meridional circulation is partially decoupled between a lower atmosphere Hadley cell-type circulation and a weaker higher altitude circulation in the same direction. The presence of the LDM appears to provide enhanced forcing for the upper circulation and accomplishes this partial decoupling. Partial decoupling is observed for nearly the entire Martian year, save near northern winter solstice when high atmospheric dust loading deepens the Hadley circulation, and more tightly integrates the upper circulation into the Hadley cell. In the simulation with a modified Conrath-ν profile (S1), the upper circulation is nearly absent throughout the year. Partial or intermediate coupling of the meridional circulations has been suggested for the Mars atmosphere following analysis of MCS observations, and *Heavens et al*. [2011c] make note of aerosol forcing as potentially a key factor in this coupling.

[23] The deeper meridional circulation that occurs with the empirical dust profile appears responsible for this improved depiction of the polar warming and the steeper slope of the polar warming toward the pole in the real atmosphere. However, additional factors may also influence the representation of the polar warming in the GCM, such as gravity wave breaking in the real atmosphere (which is not included in the current version of MarsWRF) and the "polar filtering" [*Richardson et al*., 2007] that is required to maintain numerical stability where the grid points converge at high latitudes in MarsWRF. Simulations incorporating a gravity wave parameterization, or utilizing a different numerical grid that avoids polar filtering [e.g., *Yuan et al*., 2012], would be required to assess the potential impact of these factors.

4. Impact on Tides and Waves

4.1. Migrating Thermal Tides

[24] Migrating tides are sun-synchronous tides that propagate westward with periods that are integer fractions of a solar day [*Chapman and Lindzen*, 1970]. The migrating diurnal tide (MDT) is a superposition of multiple diurnal Hough modes and is dominated by the $\Theta_1^{1,1}$ wave in the $\Theta_n^{\sigma,s}$ notation used by *Chapman and Lindzen* [1970], where σ is frequency (in cycles per solar day), s is wave number, and n is Hough

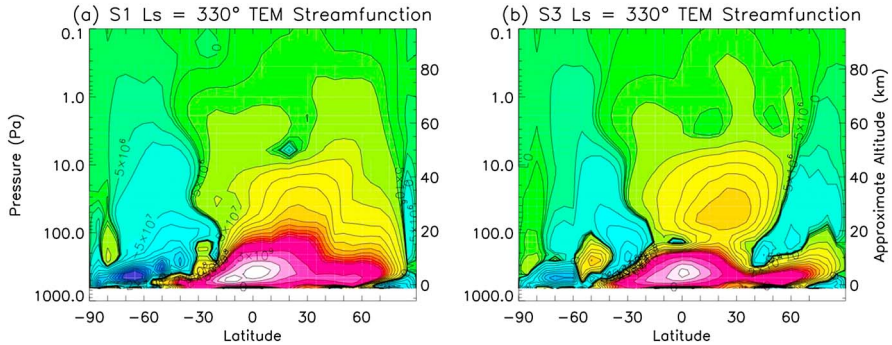

Figure 7. Transformed Eulerian Mean stream functions at $L_s = 330°$ for (a) simulation S1 and (b) simulation S3. Units are kg/s, with positive values representing clockwise motion.

mode. This $\Theta_1^{1,1}$ wave is equatorially trapped to approximately ±30°, but propagates vertically away from its forcing region (typically the surface). At more poleward latitudes, Hough modes contributing to the MDT are vertically trapped. Similarly, the migrating semidiurnal tide (MST) and migrating terdiurnal tide (MTT) are dominated by the $\Theta_2^{2,2}$ and $\Theta_3^{3,3}$ waves, respectively.

[25] The MDT has been studied through observations, modeling and theory. Observations of the MDT date back to Mariner 9 [*Hanel et al*., 1972] and have been continued with more recent orbiter missions such as Viking [*Martin and Kieffer*, 1979], MGS [*Banfield et al*., 2003], and MRO [*Lee et al*., 2009; *Guzewich et al*., 2012] as well as landed observations from the Viking landers [*Leovy and Zurek*, 1979]. Application of modeling and theory has been similarly extensive, especially in examination of the impact of dust storm conditions on the MDT [*Zurek*, 1976; *Wilson and Hamilton* 1996; *Bridger and Murphy*, 1998; *Wilson and Richardson*, 2000; *Takahashi et al*., 2006]. Aliasing concerns, associated with sun-synchronous observations, have prevented direct space-based observations of the MST and MTT with recent spacecraft, although the Viking, Mars Pathfinder, and Phoenix landers did directly observe the MST in pressure, wind, and temperature [*Tillman et al*., 1993; *Schofield et al*., 1997; *Taylor et al*., 2010] and the variable nature of Viking orbiter infrared scanning observations allowed some sampling of the full latitude-local time distribution at roughly 10–40 km altitude [*Martin*, 1981; *Wilson and Richardson*, 2000]. Like the MDT, the MST has been studied through modeling and theory [e.g., *Forbes and Miyahara*, 2006]. In brief, both the MDT and MST are strongly forced by atmospheric dust and increased dust opacity has been confidently linked to enhanced amplitudes of both migrating tides.

[26] The studies mentioned in the previous paragraph linked increased dust opacity at the surface with enhanced MDT amplitudes. MDT amplitudes near equinox are higher in our 3 year simulation S5 than in simulation S1, and analysis of simulations S1–S4 indicates this is primarily due to differences in the total column dust optical depth map, rather than the altered vertical dust profile.

[27] However, increasing dust opacity at higher altitudes also is theoretically predicted to diminish the MDT amplitudes. In comparing simulations S1–S4, the two with empirical TES vertical dust profiles (simulations S2 and S3) have lower MDT amplitudes at nearly all seasons than their counterparts with identical total column dust optical depth maps and modified Conrath-ν dust profiles. The only exception is at equinox, when the $\Theta_1^{1,1}$ mode is most strongly forced and the amplitudes are similar. In all other seasons, simulations S2 and S3 have amplitudes 30–70% lower in the equatorial middle atmosphere where the MDT amplitude is typically largest. The driver of this reduction is illustrated in the phase diagrams and seen in Figure 8. In simulations S2 and S3, the dust-forced thermotidal forcing is spread over a much larger depth of the atmosphere and the vertically propagating $\Theta_1^{1,1}$ mode is subject to destructive interference. A similar phenomenon occurs in the terrestrial atmosphere where the ozone forcing is spread over approximately 40 km while the vertical wavelength of the $\Theta_1^{1,1}$ mode on Earth is near 25 km [*Chapman and Lindzen*, 1970]. This destructive interference between the surface-forced tide and the atmospheric dust-forced tide pushes the phase transitions in the tide away from the altitude range of increased dust thermotidal forcing near 60 km (i.e., to lower and higher altitudes) in simulations S2 and S3, as demonstrated in Figure 8.

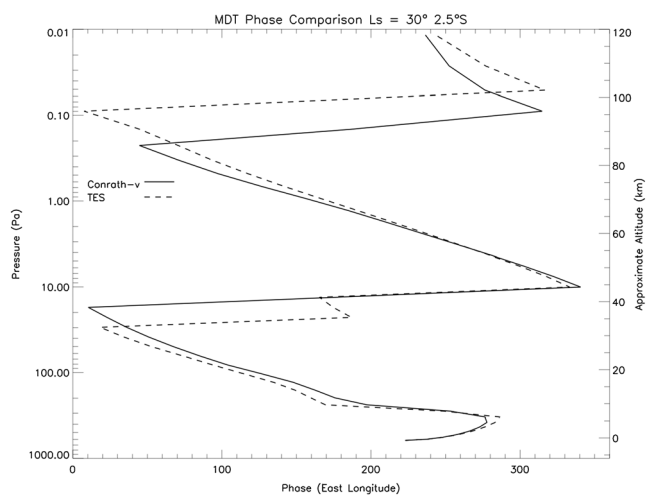

Figure 8. Phase of the migrating diurnal tide (in degrees of east longitude) at $L_s = 30°$ and 2.5°S. Dashed line represents the average of simulations S2 and S3 using the empirical TES vertical dust profile and the solid line represents the average of simulations S1 and S4 using a Conrath-ν profile.

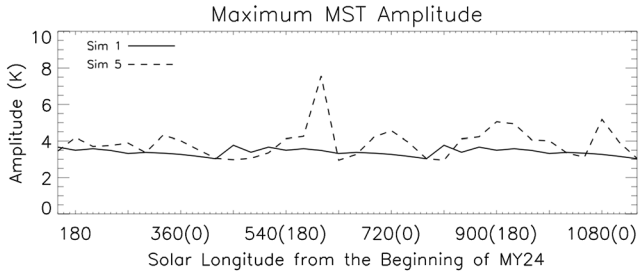

Figure 9. Comparison of the global maximum migrating semidiurnal tide temperature amplitude for simulation S1 (solid line) and simulation S5 (dashed line) over the nearly 3 MY period of simulation S5.

[28] Additionally, simulations with the empirical TES vertical profile show increased amplitude of the vertically trapped modes that contribute to the MDT at high latitudes. The enhancement of the trapped modes with increased dust opacity has been seen in previous modeling studies [*Wilson and Richardson*, 2000; *Banfield et al.*, 2003; *Forbes and Miyahara*, 2006]. During GDS01 in simulation S5, the $\Theta_1^{1,1}$ mode is not clearly present while the trapped modes exhibit amplitudes of greater than 20 K over the southern high latitudes near 40 km altitude and again near 90 km (not shown).

[29] As might be expected from theory, the MST reacts strongly to the presence of discrete layers of enhanced dust opacity at high altitudes in simulations S2, S3, and S5. Vertically extended thermal forcing in these simulations efficiently excites the MST, which possesses a very long (100 km or greater) vertical wavelength. The maximum amplitude of the MST in simulation S5 is larger than that in simulation S1 for nearly every 30° of solar longitude period (Figure 9). A prominent MST amplitude spike is seen at the time of GDS01, which compares well to that seen by *Lewis and Barker* [2005] in a GCM assimilation of TES data. The high amplitudes in S5 also span a larger volume of atmosphere than in simulation S1. In most periods of the 3 year simulation S5, amplitudes ≥1 K cover the altitude range of the lower dust maximum (20–30 km), while those amplitudes are absent in simulations using the MCD MGS/modified Conrath-ν dust scenario.

[30] By comparing simulations S1–S4, we are able to differentiate between the impact of the vertical dust profile and that of the altered horizontal distribution of total column dust optical depth. In simulations S2 and S3, with the empirical TES vertical dust profile, the gravest Hough mode ($\Theta_2^{2,2}$) dominates the tidal field and higher-order modes are confined to poleward latitudes. In simulations S1 and S4 with the modified Conrath-ν profile, the higher-order modes dominate the field even at low latitudes in the lower and middle atmosphere. Based on analysis of the phase progression, it seems the $\Theta_8^{2,2}$ mode, with a theoretical vertical wavelength near 31 km, is most clearly present. Comparing simulation S1 with S3 and simulation S2 with S4 (i.e., comparing simulations with identical total column dust optical depth maps), the simulations with the modified Conrath-ν profile (S1 and S4) exhibit generally larger MST amplitudes at high altitudes in the near-solstice seasons than the simulations with the empirical TES profile (S2 and S3). This appears to be due to the suppression of the higher-order modes in simulations S2 and S3, resulting in a net amplitude reduction. Conversely, simulations with the empirical TES profile (S2 and S3) exhibit larger amplitudes in the near-equinox seasons. The trend of larger amplitudes in the 20–30 km altitude range seen in simulation S5 was again seen in simulations S2 and S3. However, the diminished presence of the $\Theta_8^{2,2}$ mode results in modestly weaker amplitudes at high altitudes (≥60 km) in solstice seasons in all simulations with the empirical TES profile (S2, S3, and S5).

4.2. Non-migrating Thermal Tides

[31] Non-migrating tides are differentiated from migrating tides by their non-sun-synchronous propagation. They propagate westward or eastward with periods that are also integer subharmonics of a solar day. On Mars, the most prominent of these non-migrating tides are the eastward diurnal Kelvin waves. Like the migrating tides, the diurnal Kelvin waves, particularly the wave number 1 diurnal Kelvin wave (DK1), have been extensively studied observationally, theoretically and in modeling [e.g., *Wilson and Hamilton*, 1996; *Banfield et al.*, 2003]. According to tidal theory, DK1 would be dominated by the gravest equatorially symmetric $\Theta_1^{-1,1}$ Hough mode, which is nearly barotropic with height and hence possesses a vertical wavelength longer than 100 km. It is forced by the interaction of MDT with the wave number 2 component of the topography, which is the dominant component of the topography in the low latitudes. Similarly, the wave number 2 diurnal Kelvin wave (DK2) and wave number 3 diurnal Kelvin wave (DK3) are forced by the wave number 3 and wave number 4 topographic components, respectively. However, an antisymmetric mode, $\Theta_2^{-1,1}$, with a theoretical

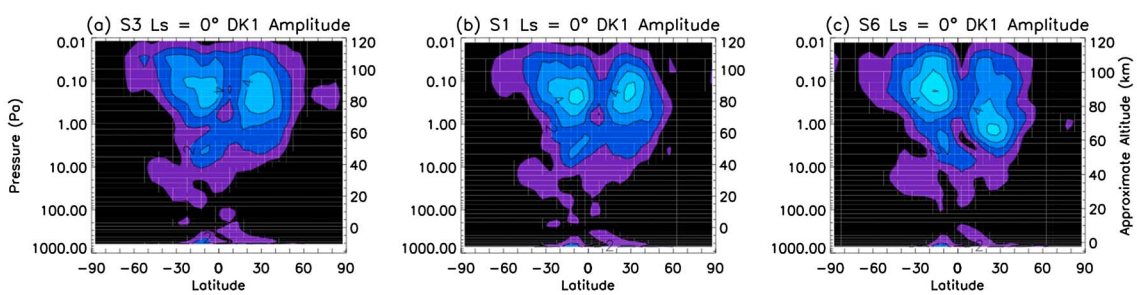

Figure 10. Diurnal Kelvin wave 1 temperature amplitude comparison for (a) simulation S3, (b) simulation S1, and (c) simulation S6.

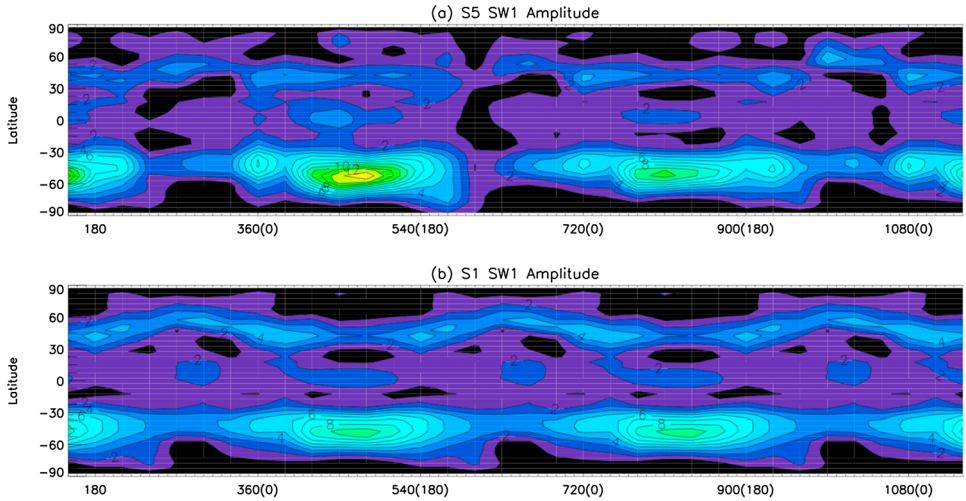

Figure 11. Amplitude (Kelvin) of the wave number 1 stationary planetary wave at the 40 Pa pressure level for (a) simulation S5 and (b) simulation S1 versus solar longitude.

vertical wavelength of 61 km, has also been seen in observations to contribute to DK1 [*Guzewich et al*., 2012].

[32] DK1 has been observed in all manner of Mars atmospheric measurements, from the Viking landers [e.g., *Leovy*, 1981; *Wilson and Hamilton*, 1996], MGS TES [e.g., *Wilson*, 2000; *Banfield et al*., 2003], to MGS aerobraking [e.g., *Wilson*, 2002] and MCS [*Guzewich et al*., 2012]. Modeling and theoretical studies of DK1 and its interaction with airborne dust have been done by, e.g., *Leovy and Zurek* [1979] and *Wilson and Hamilton* [1996]. DK1 is near resonance in the clear-air or low-dust Martian atmosphere, due to the close match of the average Martian atmospheric scale height and the $\Theta_1^{-1,1}$ Hough mode's equivalent depth (both near 11 km). The presence of airborne dust pushes DK1 away from resonance by extending the atmospheric scale height. However, added dust also increases atmospheric heating and enhances the MDT. Therefore, modeling and theoretical studies suggest that DK1's amplitude should be relatively constant with varying atmospheric dust levels.

[33] During GDS01 during simulation S5, the amplitudes of the diurnal Kelvin waves drop to nearly zero. *Zurek and Leovy* [1981] postulated that the absence of the migrating diurnal pressure tide in Viking lander measurements during the second 1977 global dust storm was due to destructive interference between an enhanced eastward propagating diurnal Kelvin wave and westward propagating migrating diurnal tide. The $\Theta_1^{1,1}$ mode of the MDT also has very low amplitude during the GDS01 simulation, with the vertically trapped modes dominant (see section 4.1). Despite the Viking observations, it appears in this case that the diminishing $\Theta_1^{1,1}$ mode similarly diminishes the diurnal Kelvin waves.

[34] In Figure 10, we compare the amplitude of DK1 in 3 simulations with varying dust vertical distributions: simulations S1, S3, and S6. As just mentioned, previous studies suggest that the amplitude should be relatively invariant to dust distributions and optical depth and this indeed appears to be the case. Our simulations show a slight decrease in DK1 amplitude when dust is introduced into the atmosphere (from S6 to S1) and another decrease beyond that with an empirical TES dust profile (from S1 to S3), but in total this only amounts to approximately 1 K on average. Still, the modeled DK1 temperature amplitudes are modestly greater in all simulations than observed amplitudes [*Guzewich et al*., 2012; *Banfield et al*., 2003] by 1–2 K, particularly in the middle atmosphere.

[35] The increased low-latitude easterly winds, in simulations with an empirical TES vertical dust profile, impacts DK3, which has an easterly phase speed of 80.2 m/s. In simulation S1, easterly winds reach that speed only near and immediately after northern winter solstice ($L_s = 270$–$300°$). In simulation S5, winds equal and surpass DK3's phase speed far more frequently in the tropical middle and upper atmosphere. As expected from theory, when the easterly propagating DK3 encounters easterly winds of equal or greater speed, the tide breaks. Hence, for approximately half of the year, DK3 is significantly weakened (by 50% or more) and has its vertical and horizontal extent reduced. This zonal wind speed wave breaking criterion is rarely met for other tides in the Martian atmosphere, although convective instability can induce wave breaking as well.

4.3. Stationary Planetary Waves

[36] Mars' dramatic topography and prevailing mid-latitude westerly winds generate large magnitude (>10 K and 1 km of geopotential height) stationary planetary waves [*Hollingsworth and Barnes*, 1996; *Hinson et al*., 2003; *Banfield et al*., 2003; *Guzewich et al*., 2012]. The southern hemisphere topography is dominated by Hellas Basin, a deep impact basin more than 7 km below the Martian datum at its deepest, and the difference between Hellas and the western hemisphere high terrain of Solis Planum and Aonia Terra is more than 10 km. This general wave number 1 (s = 1) topography of the southern hemisphere forces the $s = 1$ planetary wave (SW1) most strongly [*Hinson et al*., 2001; *Hinson et al*., 2003; *Banfield et al*., 2003; *Guzewich et al*., 2012]. In contrast, the northern hemisphere has a dominant $s = 2$ topography, represented by the highlands of Arabia Terra and Alba Patera and the low plains of Acidalia, Arcadia, and Utopia Planitias, resulting in a preferential forcing of the $s = 2$ planetary wave (SW2).

[37] In the southern hemisphere, SW1 peaks in amplitude near winter solstice ($L_s = 90°$). The wave is ducted along the axis of the strong westerly jet stream at this season, from near the surface to above the 1 Pa pressure level. The seminal work of *Charney and Drazin* [1961] found that vertical planetary wave propagation occurs when winds are weakly westerly and that low wave number waves can propagate higher in the atmosphere. However, while this is broadly consistent with terrestrial (and Martian) observations of wintertime wave propagation and summertime suppression, planetary waves clearly propagate through areas of strong westerly winds. The ducting phenomenon was first articulated by *Matsuno* [1970] and describes the utility of the quasi-geostrophic index of refraction in defining the region of wave vertical propagation as well as the direction (e.g., poleward or equatorward) of a wave's raypath. As seen in Figure 11 (plotted at 40 Pa pressure level), the temperature amplitude of SW1 in simulation S5 is as much as 4 K higher than in simulation S1 near southern winter solstice. Conversely, the wave is 2 K weaker in simulation S5 compared to S1 in the northern hemisphere, where the wave is not as strongly forced. As mentioned in section 3.1, the jet stream is stronger in simulation S5 (and in the other simulations with an empirical TES vertical profile) than in simulation S1. Additionally, it is shifted poleward by 2–5° of latitude in the solstice seasons. This tightens the horizontal gradient of potential vorticity on the poleward side of the jet stream and hence increases the gradient of the quasi-geostrophic index of refraction on the poleward flank of the jet. Quasi-geostrophy is not applicable in all situations on Mars, particularly near the core of jet streams where the Rossby number is high. However, the Rossby number is low on the flanks of the jets and in low wind speed environments. The stronger gradient of the quasi-geostrophic index of refraction in simulation S5 causes SW1 to be both enhanced in amplitude and reflected poleward more readily [*Nigam and Lindzen*, 1989]. Additionally, the stronger jet speed and latitudinal shift impact SW1 similarly [*Lin*, 1982; *Nigam and Lindzen*, 1989]. In the northern hemisphere, the poleward gradient of quasi-geostrophic index of refraction is weakened and the SW1 amplitude is slightly reduced. This pattern is seen again in comparing simulation S6 (dust-free) with simulation S1. The jet stream is 20–40 m/s weaker in simulation S6, and SW1 exhibits a markedly different structure (less ducting along the jet) and 2–3 K weaker amplitudes.

[38] The Charney-Drazin criteria are more applicable for SW2 and SW3. Even in simulation S1, they do not propagate as high vertically as SW1 and that trend continues in simulation S5, where those waves remain even more trapped near the surface. SW2 and SW3 do not get ducted into the jet and high amplitudes remain outside of the high speed wind cores.

5. Conclusions

[39] We forced the MarsWRF GCM using two versions of a dust climatology developed from 3 Mars years of TES limb-scanning dust observations [*Guzewich et al.*, 2013]. The first version is an "average year" compiled from the 3 year data set, while the second is an evolving multiyear version that "plays" the full 3 years of the dust climatology through the model forcing. We conducted six MarsWRF simulations (see Table 1) and examined the results to determine the impact of the vertical dust profile on the general circulation of the atmosphere, thermal tides, and planetary waves. The empirical TES vertical dust profile described in *Guzewich et al*. [2013] is characterized by the presence of two discrete layers of enhanced dust mixing ratio and opacity. The lowermost is between 20 and 30 km and the uppermost is found at 45–65 km altitude. This empirical profile was compared to simulations using the canonical Conrath-ν vertical dust profile that represents a balance between vertical eddy mixing and gravitational sedimentation [*Conrath*, 1975], which has found widespread use in the Mars GCM community.

[40] The simulated temperatures in model simulation S5 using the TES dust climatology more closely matched TES temperature observations by more than 1 standard deviation over our "standard" simulation S1 using the MCD MGS/modified Conrath-ν dust scenario. Most of the improvement came from an improved depiction of the polar warming (in both amplitude and location) and a warmer tropical lower atmosphere that more closely matches TES observations. However, the tropical middle atmosphere is significantly too warm in our simulations using an empirical TES vertical dust profile, which may reflect the role of stronger adiabatic cooling in the real atmosphere or water ice clouds that are not treated in this study. Through the thermal wind relation, the increased horizontal temperature gradient in the polar warming and tropical atmosphere results in a strengthened westerly jet stream at middle and high latitudes. The jet is also shifted poleward by 2–5° of latitude.

[41] The presence of increased dust opacity at high altitudes partially decouples the lower atmospheric meridional overturning circulation (Hadley circulation) from a middle at mospheric cell. This results in increased adiabatic downwelling at the poles, particularly at northern winter solstice, producing a 20–30 K warmer polar warming inversion above the high northern latitudes. Indeed, this polar temperature inversion is occasionally stronger than TES observations indicate, but indicates the importance of a realistic vertical dust profile in accurately depicting this key feature of the Martian atmosphere, possibly in conjunction with the depiction of radiatively active water ice clouds [*Wilson et al*., 2008; *Madeleine et al*., 2012].

[42] The vertical dust profile also impacts atmospheric waves. The migrating diurnal (MDT) and semidiurnal tides (MST) react strongly to the presence of dust at higher altitudes. The increased altitude span with significant thermotidal forcing fosters destructive interference of the MDT, with the wave being forced over a deeper portion of the atmosphere. This results in 30–70% decrease in tropical tidal temperature amplitudes, particularly outside of the equinox seasons when the MDT is most efficiently excited. The gravest Hough mode contributing to the MST is enhanced by the presence of a deeper dust column in the atmosphere, but this serves to weaken higher-order modes that contribute to the MST substantially in simulations with a modified Conrath-ν vertical dust profile. The eastward wave number 1 diurnal Kelvin wave is affected in a limited manner by the altered vertical dust profile, as suggested by tidal theory. The wave number 3 eastward diurnal Kelvin wave is subject to wave breaking more readily in simulations with the empirical TES dust profile, as tropical easterly winds are often stronger at lower altitudes.

[43] Lastly, the wave number 1 stationary planetary wave is stronger by up to 4 K in the southern hemisphere in simulations with an empirical TES vertical dust profile. This increase is forced by the stronger westerly winds in the polar jet duct in which the wave propagates and by a sharpened gradient in the quasi-geostrophic index of refraction on the poleward flank of the jet. The wave number 2 and 3 stationary waves show limited changes between the simulations with the alternate dust profiles, as they appear to be more affected by the Charney-Drazin criteria for vertical propagation.

[44] In summary, the vertical dust profile is a major determinant of atmospheric forcing on Mars, but one that has not been conducive to study until very recently due to the lack of systematic observations. This work is an attempt to diagnose the importance of the vertical dust profile on large-scale atmospheric features by taking advantage of new retrievals from TES limb observations. These observations by TES, along with MCS retrievals, indicate that the traditional and modified Conrath-ν vertical dust profile does not accurately represent the true vertical dust profile, particularly in the low latitudes. Our results suggest a significant improvement of model simulation of air temperatures and wave components as compared to existing forcing prescriptions. We determine that the vertical dust profile plays a large role in controlling or modifying many of the features of the Martian atmosphere, including the polar warmings, Hadley circulation, and thermal tides. While the dust climatology and average vertical dust profile used herein can only be taken to be representative of MY 24–27, all extant climatological forcing prescriptions [e.g., *Montmessin et al.*, 2004] are also limited by the very short baseline of spacecraft observations. As such, the forcing of models using the TES limb climatology is an attractive alternative to these standard climatologies. In either case, the vertical dust profile is a factor that must be considered in future GCM studies of the Martian atmosphere. Future work is also needed to extend the climatology to include MCS observations and to treat climatological observations of water ice opacity in addition to dust.

[45] **Acknowledgments.** This work was funded by a Johns Hopkins University Applied Physics Laboratory graduate student fellowship. We thank R. John Wilson and Jean-Baptiste Madeleine for helpful reviews which have improved and clarified this work.

References

Andrews, D. G., and M. E. McIntyre (1976), Planetary waves in horizontal and vertical shear: The generalized Eliassen–Palm relation and the mean zonal acceleration, *J. Atmos. Sci.*, *33*, 2031–2048.

Banfield, D., B. Conrath, M. D. Smith, P. R. Christensen, and R. J. Wilson (2003), Forced waves in the Martian atmosphere from MGS TES nadir data, *Icarus*, *161*(2), 319–345, doi:10.1016/S0019-1035(02)00044-1.

Basu, S., M. I. Richardson, and R. J. Wilson (2004), Simulation of the Martian dust cycle with the GFDL Mars GCM, *J. Geophys. Res.*, *109*, E11006, doi:10.1029/2004JE002243.

Bell, J. M., S. W. Bougher, and J. R. Murphy (2007), Vertical dust mixing and the interannual variations in the Mars thermosphere, *J. Geophys. Res.*, *112*, E12002, doi:10.1029/2006JE002856.

Bridger, A. F. C., and J. R. Murphy (1998), Mars' surface pressure tides and their behavior during global dust storms, *J. Geophys. Res.*, *103*(E4), 8587–8601, doi:10.1029/98JE00242.

Briegleb, B. P. (1992), Longwave band model for thermal radiation in climate studies, *J. Geophys. Res.*, *97*(D11), 11,475–11,485, doi:10.1029/92JD00806.

Chapman, S., and R. S. Lindzen (1970), *Atmospheric Tides*, D. Reidel, Norwell, Mass.

Charney, J. G., and P. G. Drazin (1961), Propagation of planetary scale disturbances from the lower into the upper atmosphere, *J. Geophys. Res.*, *66*, 83–109.

Clancy, R. T., S. W. Lee, G. R. Gladstone, W. W. McMillan, and T. Rousch (1995), A new model for Mars atmospheric dust based upon analysis of ultraviolet through infrared observations from Mariner 9, Viking, and Phobos, *J. Geophys. Res.*, *100*(E3), 5251–5263, doi:10.1029/94JE01885.

Clancy, R. T., M. J. Wolff, B. A. Whitney, B. A. Cantor, M. D. Smith, and T. H. McConnochie (2010), Extension of atmospheric dust loading to high altitudes during the 2001 Mars dust storm: MGS TES limb observations, *Icarus*, *207*, 98–109.

Colburn, D. S., J. B. Pollack, and R. M. Haberle (1989), Diurnal variations in optical depth at Mars, *Icarus*, *79*(1), 159–189, doi:10.1016/0019-1035(89)90114-0.

Conrath, B. J. (1975), Thermal structure of the Martian atmosphere during the dissipation of the dust storm of 1971, *Icarus*, *24*, 36–46.

Deming, D., M. J. Mumma, F. Espenak, T. Kostiuk, and D. Zipoy (1986), Polar warming in the middle atmosphere of Mars, *Icarus*, *66*(2), 366–379, doi:10.1016/0019-1035(86)90165-X.

Forbes, J. M., and S. Miyahara (2006), Solar semidiurnal tide in the dusty atmosphere of Mars, *J. Atmos. Sci.*, *63*, 1798–1817, doi:http://dx.doi.org/10.1175/JAS3718.1

Forget, F., F. Hourdin, R. Fournier, C. Hourdin, O. Talagrand, M. Collins, S. R. Lewis, P. L. Read, and J.-P. Huot (1999), Improved general circulation models of the Martian atmosphere from the surface to above 80 km, *J. Geophys. Res.*, *104*(E10), 24,155–24,175, doi:10.1029/1999JE001025.

Greybush, S. J., R. Wilson, R. N. Hoffman, M. J. Hoffman, T. Miyoshi, K. Ide, T. McConnochie, and E. Kalnay (2012), Ensemble Kalman Filter data assimilation of Thermal Emission Spectrometer (TES) temperature retrievals into a Mars GCM, *J. Geophys. Res.*, *117*, E11008, doi:10.1029/2012JE004097.

Guzewich, S. D., E. R. Talaat, A. D. Toigo, D. W. Waugh, and T. H. McConnochie (2013), High altitude dust layers: Observations with the thermal emission spectrometer, *J. Geophys. Res.*, *118*, doi:10.1002/jgre.20076.

Guzewich, S. D., E. R. Talaat, and D. W. Waugh (2012), Observations of planetary waves and nonmigrating tides by the Mars Climate Sounder, *J. Geophys. Res.*, *117*, E03010, doi:10.1029/2011JE003924.

Haberle, R. M., C. B. Leovy, and J. M. Pollack (1982), Some effects of global dust storms on the atmospheric circulation of Mars, *Icarus*, *50*, 322–367, doi:10.1016/0019-1035(82)90129-4.

Haberle, R. M., J. B. Pollack, J. R. Barnes, R. W. Zurek, C. B. Leovy, J. R. Murphy, H. Lee, and J. Schaeffer (1993), Mars atmospheric dynamics as simulated by the NASA Ames General Circulation Model 1. The zonal-mean circulation, *J. Geophys. Res.*, *98*(E2), 3093–3123, doi:10.1029/92JE02946.

Hanel, R., et al. (1972), Investigation of the Martian environment by infrared spectroscopy on Mariner 9, *Icarus*, *17*(2), 423–442, doi:10.1016/0019-1035(72)90009-7.

Heavens, N. G., M. I. Richardson, A. Kleinböhl, D. M. Kass, D. J. McCleese, W. Abdou, J. L. Benson, J. T. Schofield, J. H. Shirley, and P. M. Wolkenberg (2011a), Vertical distribution of dust in the Martian atmosphere during northern spring and summer: High-altitude tropical dust maximum at northern summer solstice, *J. Geophys. Res.*, *116*, E01007, doi:10.1029/2010JE003692.

Heavens, N. G., M. I. Richardson, A. Kleinböhl, D. M. Kass, D. J. McCleese, W. Abdou, J. L. Benson, J. T. Schofield, J. H. Shirley, and P. M. Wolkenberg (2011b), The vertical distribution of dust in the Martian atmosphere during northern spring and summer: Observations by the Mars Climate Sounder and analysis of zonal average vertical dust profiles, *J. Geophys. Res.*, *116*, E04003, doi:10.1029/2010JE003691.

Heavens, N. G., D. J. McCleese, M. I. Richardson, D. M. Kass, A. Kleinböhl, and J. T. Schofield (2011c), Structure and dynamics of the Martian lower and middle atmosphere as observed by the Mars Climate Sounder: 2. Implications of the thermal structure and aerosol distributions for the mean meridional circulation, *J. Geophys. Res.*, *116*, E01010, doi:10.1029/2010JE003713.

Hinson, D., G. Tyler, J. Hollingsworth, and R. Wilson (2001), Radio occultation measurements of forced atmospheric waves on Mars, *J. Geophys. Res.*, *106*(E1), 1463–1480.

Hinson, D. P., R. J. Wilson, M. D. Smith, and B. J. Conrath (2003), Stationary planetary waves in the atmosphere of Mars during southern winter, *J. Geophys. Res.*, *108*(E1), 5004, doi:10.1029/2002JE001949.

Hollingsworth, J. L., and J. R. Barnes (1996), Forced stationary planetary waves in Mars's winter atmosphere, *J. Atmos. Sci.*, *53*, 428–448, doi:10.1175/1520-0469(1996)053<0428:FSPWIM>2.0.CO;2.

Hourdin, F. (1992), A new representation of the absorption by the CO_2 15-μm band for a Martian general circulation model, *J. Geophys. Res.*, *97*(E11), 18,319–18,335, doi:10.1029/92JE01985.

Jakosky, B. M., and T. Z. Martin (1987), Mars: North-polar atmospheric warning during dust storms, *Icarus*, *72*(3), 528–534, doi:10.1016/0019-1035(87)90050-9.

Kahre, M. A., J. L. Hollingsworth, R. M. Haberle, and J. R. Murphy (2008), Investigations of the variability of dust particle sizes in the Martian atmosphere using the NASA Ames General Circulation Model, *Icarus*, *195*, 576–597, doi:10.1016/j.icarus.2008.01.023.

Kahre, M. A., J. R. Murphy, and R. M. Haberle (2006), Modeling the Martian dust cycle and surface dust reservoirs with the NASA Ames general circulation model, *J. Geophys. Res.*, *111*, E06008, doi:10.1029/2005JE002588.

Kuroda, T., A. S. Medvedev, P. Hartogh, and M. Takahashi (2009), On forcing the winter polar warmings in the Martian middle atmosphere during dust storms, *J. Meteorol. Soc. Jpn.*, *87*, 913–921, doi:10.2151/jmsj.87.913.

Lee, C., et al. (2009), Thermal tides in the Martian middle atmosphere as seen by the Mars Climate Sounder, *J. Geophys. Res.*, *114*, E03005, doi:10.1029/2008JE003285.

Leovy, C. B., G. A. Briggs, A. T. Young, B. A. Smith, J. B. Pollack, E. N. Shipley, and R. L. Wildey (1972), The Martian atmosphere: Mariner 9 television experiment progress report, *Icarus*, *17*, 373–393.

Leovy, C. B., and R. W. Zurek (1979), Thermal tides and Martian dust storms: Direct evidence for coupling, *J. Geophys. Res.*, *84*(B6), 2956–2968, doi:10.1029/JB084iB06p02956.

Leovy, C. B. (1981), Observations of Martian tides over two annual cycles, *J. Atmos. Sci.*, *38*, 30–39, doi:10.1175/1520-0469(1981)038<0030:OOMTOT>2.0.CO;2.

Lewis, S. R., M. Collins, P. L. Read, F. Forget, F. Hourdin, R. Fournier, C. Hourdin, O. Talagrand, and J. P. Huot (1999), A climate data base for Mars, *J. Geophys. Res.*, *104*(E10), 24177–24194.

Lewis, S. R., and P. R. Barker (2005), Atmospheric tides in a Mars general circulation model with data assimilation, *Adv. Space Res.*, *36*(11), 2162–2168, doi:10.1016/j.asr.2005.05.122.

Lin, B.-D. (1982), The behavior of winter stationary planetary waves forced by topography and diabatic heating, *J. Atmos. Sci.*, *39*, 1206–1226.

Madeleine, J.-B., F. Forget, E. Millour, T. Navarro, and A. Spiga (2012), The influence of radiatively active water ice clouds on the Martian climate, *Geophys. Res. Lett.*, *39*, L23202, doi:10.1029/2012GL053564.

Madeleine, J.-B., F. Forget, E. Millour, L. Montabone, and M. J. Wolff (2011), Revisiting the radiative impact of dust on Mars using the LMD Global Climate Model, *J. Geophys. Res.*, *116*, E11010, doi:10.1029/2011JE003855.

Martin, T. Z., and H. H. Kieffer (1979), Thermal infrared properties of the Martian atmosphere 2. The 15-μm band measurements, *J. Geophys. Res.*, *84*(B6), 2843–2852, doi:10.1029/JB084iB06p02843.

Martin, T. Z. (1981), Mean thermal and albedo behavior of the Mars surface and atmosphere over a Martian year, *Icarus*, *45*(2), 427–446, doi:10.1016/0019-1035(81)90045-2.

Matsuno, T. (1970), Vertical propagation of stationary planetary waves in the winter northern hemisphere, *J. Atmos. Sci.*, *27*, 871–883.

McCleese, D. J., et al. (2008), Intense polar temperature inversion in the middle atmosphere on Mars, *Nature*, *1*, 745–749, doi:10.1038/ngeo332.

McCleese, D. J., et al. (2010), The structure and dynamics of the Martian lower and middle atmosphere as observed by the Mars Climate Sounder: 1. Seasonal variations in zonal mean temperature, dust and water ice aerosols, *J. Geophys. Res.*, *115*, E12016, doi:10.1029/2010JE003677.

McDunn, T. L., S. W. Bougher, A. Kleinböhl, F. Forget, J. R. Murphy, M. D., and M. A. Mischna (2011), Middle atmosphere polar warming at Mars, presented at the Fall 2011 American Geophysical Union Meeting, abstract SP23E-09.

Mischna, M. A., C. Lee, and M. Richardson (2012), Development of a fast, accurate radiative transfer model for the Martian atmosphere, past and present, *J. Geophys. Res.*, *117*, E10009, doi:10.1029/2012JE004110.

Montmessin, F., F. Forget, P. Rannou, M. Cabane, and R. M. Haberle (2004), Origin and role of water ice clouds in the Martian water cycle as inferred from a general circulation model, *J. Geophys. Res.*, *109*, E10004, doi:10.1029/2004JE002284.

Murphy, J. R., R. M. Haberle, O. B. Toon, and J. B. Pollack (1993), Martian global dust storms—Zonally symmetric numerical simulations including size-dependent particle transport, *J. Geophys. Res.*, *98*(E2), 3197–3220, doi:10.1029/92JE02945.

Newman, C. E., S. R. Lewis, P. L. Read, and F. Forget (2002a), Modeling the Martian dust cycle: 1. Representations of dust transport processes, *J. Geophys. Res.*, *107*(E12), 5123, doi:10.1029/2002JE001910.

Newman, C. E., S. R. Lewis, P. L. Read, and F. Forget (2002b), Modeling the Martian dust cycle: 2. Multiannual radiatively active dust transport simulations, *J. Geophys. Res.*, *107*(E12), 5124, doi:10.1029/2002JE001920.

Nigam, S., and R. S. Lindzen (1989), The sensitivity of stationary waves to variations in the basic state zonal flow, *J. Atmos. Sci.*, *46*, 1746–1768, doi: http://dx.doi.org/10.1175/1520-0469(1989)046<1746:TSOSWT>2.0.CO;2

Pollack, J. B., D. S. Colburn, F. M. Flasar, R. Kahn, C. E. Carlston, and D. Pidek (1979), Properties and effects of dust particles suspended in the Martian atmosphere, *J. Geophys. Res.*, *84*(B6), 2929–2945, doi:10.1029/JB084iB06p02929.

Richardson, M. I., A. D. Toigo, and C. E. Newman (2007), PlanetWRF: A general purpose, local to global numerical model for planetary atmospheric and climate dynamics, *J. Geophys. Res.*, *112*, E09001, doi:10.1029/2006JE002825.

Richardson, M. I., and R. J. Wilson (2002), A topographically forced asymmetry in the Martian circulation and climate, *Nature*, *416*, 298–301, doi:10.1038/416298a.

Sagan, C., and J. B. Pollack (1969), Windblown dust on Mars, *Nature*, *223*, 791–794.

Schofield, J. T., J. R. Barnes, D. Crisp, R. M. Haberle, S. Larsen, J. A. Magalhaes, J. R. Murphy, A. Seiff, and G. Wilson (1997), The Mars Pathfinder Atmospheric Structure Investigation (ASI/MET) Meteorological Experiment, *Science*, *278*, 1752–1758, doi:10.1126/science.278.5344.1752.

Smith, M. D., J. C. Pearl, B. J. Conrath, and P. R. Christensen (2001), Thermal Emission Spectrometer results: Mars atmospheric thermal structure and aerosol distribution, *J. Geophys. Res.*, *106*(E10), 23,929–23,945, doi:10.1029/2000JE001321.

Smith, M. D. (2004), Interannual variability in TES atmospheric observations of Mars during 1999–2003, *Icarus*, *167*, 148–165, doi:10.1016/j.icarus.2003.09.010.

Takahashi, Y. O., H. Fujiwara, and H. Fukunishi (2006), Vertical and latitudinal structure of the migrating diurnal tide in the Martian atmosphere: Numerical investigations, *J. Geophys. Res.*, *111*, E01003, doi:10.1029/2005JE002543.

Taylor, P. A., et al. (2010), On pressure measurement and seasonal pressure variations during the Phoenix mission, *J. Geophys. Res.*, *115*, E00E15, doi:10.1029/2009JE003422.

Tillman, J. E., N. C. Johnson, P. Guttorp, and D. B. Percival (1993), The Martian annual atmospheric pressure cycle: Years without great dust storms, *J. Geophys. Res.*, *98*(E6), 10,963–10,971, doi:10.1029/93JE01084.

Toigo, A., C. Lee, C. E. Newman, and M. I. Richardson (2012), The impact of resolution on the dynamics of the Martian global atmosphere: Varying resolution studies with the MarsWRF GCM, *Icarus*, *221*(1), 276–288, doi:10.1016/j.icarus/2012.07.020.

Toigo, A. D., and M. I. Richardson (2002), A mesoscale model for the Martian atmosphere, *J. Geophys. Res.*, *107*(E7), 5049, doi:10.1029/2000JE001489.

Wilson, R. J., and K. Hamilton (1996), Comprehensive model simulation of thermal tides in the Martian atmosphere, *J. Atmos. Sci.*, *53*, 1290–1326, doi:10.1175/1520-0469(1996)053<1290:CMSOTT>2.0.CO;2.

Wilson, R. J. (1997), A general circulation model simulation of the Martian polar warming, *Geophys. Res. Lett.*, *24*(2), 123–126, doi:10.1029/96GL03814.

Wilson, R. J., and M. I. Richardson (2000), The Martian atmosphere during the Viking Mission, I: Infrared measurements of atmospheric temperatures revisited, *Icarus*, *145*, 555–579, doi:10.1006/icar.2000.6378.

Wilson, R. J. (2000), Evidence for diurnal period Kelvin waves in the Martian atmosphere from Mars Global Surveyor TES data, *Geophys. Res. Lett.*, *27*(23), 3889–3892.

Wilson, R. J. (2002), Evidence for nonmigrating thermal tides in the Mars upper atmosphere from the Mars Global Surveyor Accelerometer Experiment, *Geophys. Res. Lett.*, *29*(7), 1120, doi:10.1029/2000GL012028.

Wilson, R. J., S. R. Lewis, L. Montabone, and M. D. Smith (2008), Influence of water ice clouds on Martian tropical atmospheric temperatures, *Geophys. Res. Lett.*, *35*, L07202, doi:10.1029/2007GL032405.

Wilson, R. J. (2011), Water ice clouds and thermal structure in the Martian tropics as revealed by Mars Climate Sounder, in *Fourth International Workshop on the Mars Atmosphere: Modelling and Observations*, Lab. de Meteorol. Dyn, Paris, France, pp. 219–222 .

Wolff, M. J., M. D. Smith, R. T. Clancy, R. Arvidson, M. Kahre, F. Seelos IV, S. Murchie, and H. Savijarvi (2009), Wavelength dependence of dust aerosol single scattering albedo as observed by the Compact Reconnaissance Imaging Spectrometer, *J. Geophys. Res.*, *114*, E00D04, doi:10.1029/2009JE003350.

Yuan, L., M. I. Richardson, C. E. Newman, C. Lee, A. D. Toigo, M. A. Mischna, and J.-M. Campin (2012), The Ashima/MIT Mars GCM and argon in the Martian atmosphere, *Icarus*, *218*(2), 1043–1070, doi:10.1016/j.icarus.2012.02.012.

Zurek, R. W. (1976), Diurnal tide in the Martian atmosphere, *J. Atmos. Sci.*, *33*, 321–337, doi:10.1175/1520-0469(1976)033.

Zurek, R., and C. B. Leovy (1981), Thermal tides in the dusty Martian atmosphere: A verification of theory, *Science*, *213*, 437–439, doi:10.1126/science.213.4506.437.